Special Issue Article

Institution of MECHANICAL ENGINEERS
Journal of ENGINEERING IN MEDICINE

Proc IMechE Part H:
J Engineering in Medicine
2020, Vol. 234(11) 1209–1222

DOI: 10.1177/0954411920923253
journals.sagepub.com/home/pih
SAGE

# Exploring wall shear stress spatiotemporal heterogeneity in coronary arteries combining correlation-based analysis and complex networks with computational hemodynamics

**Karol Calò[1], Giuseppe De Nisco[1], Diego Gallo[1], Claudio Chiastra[1], Ayla Hoogendoorn[2], David A Steinman[3], Stefania Scarsoglio[1], Jolanda J Wentzel[2] and Umberto Morbiducci[1]**

## Abstract

Atherosclerosis at the early stage in coronary arteries has been associated with low cycle-average wall shear stress magnitude. However, parallel to the identification of an established active role for low wall shear stress in the onset/progression of the atherosclerotic disease, a weak association between lesions localization and low/oscillatory wall shear stress has been observed. In the attempt to fully identify the wall shear stress phenotype triggering early atherosclerosis in coronary arteries, this exploratory study aims at enriching the characterization of wall shear stress emerging features combining correlation-based analysis and complex networks theory with computational hemodynamics. The final goal is the characterization of the spatiotemporal and topological heterogeneity of wall shear stress waveforms along the cardiac cycle. In detail, here time-histories of wall shear stress magnitude and wall shear stress projection along the main flow direction and orthogonal to it (a measure of wall shear stress multidirectionality) are analyzed in a representative dataset of 10 left anterior descending pig coronary artery computational hemodynamics models. Among the main findings, we report that the proposed analysis quantitatively demonstrates that the model-specific inlet flow-rate shapes wall shear stress time-histories. Moreover, it emerges that a combined effect of low wall shear stress magnitude and of the shape of the wall shear stress–based descriptors time-histories could trigger atherosclerosis at its earliest stage. The findings of this work suggest for new experiments to provide a clearer determination of the wall shear stress phenotype which is at the basis of the so-called arterial hemodynamic risk hypothesis in coronary arteries.

## Keywords

Computational fluid dynamics, complex networks, spatiotemporal analysis, wall shear stress, coronary artery

Date received: 17 October 2019; accepted: 7 April 2020

## Introduction

Atherosclerosis is an inflammatory disease of the arterial system that represents the main cause of coronary artery disease. Atherosclerotic plaques growth produces the narrowing or blockage of the coronary arteries ultimately leading to a reduced perfusion of the heart. According to the "hemodynamic risk hypothesis",[1] local hemodynamics, in particular wall shear stress (**WSS**), are involved in the onset and progression of the atherosclerotic disease. A large body of literature attributed the preferential development of the disease in

[1]PoliTo[BIO]Med Lab, Department of Mechanical and Aerospace Engineering, Politecnico di Torino, Turin, Italy
[2]Department of Cardiology, Biomedical Engineering, Erasmus MC, Rotterdam, The Netherlands
[3]Biomedical Simulation Lab, Department of Mechanical & Industrial Engineering, University of Toronto, Toronto, ON, Canada

**Corresponding author:**
Umberto Morbiducci, PoliTo[BIO]Med Lab, Department of Mechanical and Aerospace Engineering, Politecnico di Torino, Corso Duca degli Abruzzi, 24, 10129 Turin, Italy.
Email: umberto.morbiducci@polito.it

arteries to low and oscillatory **WSS** phenotype.[2–4] However, more recent findings highlighted that (1) low WSS is a significant but moderately weak predictor of atherosclerotic plaque development,[5,6] and that (2) hemodynamic descriptors based only upon **WSS** magnitude and/or direction do not properly account for the complex hemodynamic milieu to which the luminal surface is exposed.[7,8] The need to bridge this gap of knowledge and identify a stronger **WSS** phenotype of arterial disease was recently stimulated by evidences on the relation between flow directionality and endothelial cells (ECs) mechanosensing,[7,9,10] and on the emergent **WSS** multidirectional nature in arteries.[11–13] In this context, an in-depth analysis of the **WSS** spatiotemporal complexity in coronary arteries is still lacking and might support the identification of emergent features in **WSS** dynamics along the cardiac cycle.

Moving along this research line, this exploratory study aims at enriching the knowledge of arterial **WSS** phenotype, investigating the existence of correlated spatiotemporal dynamics of **WSS** magnitude along the cardiac cycle in coronary arteries, because of its suggested role (in terms of cycle-average quantity) in the causation of the disease process.[6,14,15] Moreover, inspired by recent observations on ECs sensing to flow multidirectionality,[7,9,10,16–18] we extended the analysis to the time-histories, that is, the waveforms along the cardiac cycle, of **WSS** vector projections along main directions based on geometric attributes of the vasculature and inspired by fluid mechanics.[11]

Technically, a correlation analysis was performed and the Complex Networks (CNs) theory was applied here for the first time to a dataset of 10 realistic computational hemodynamics models of pig left anterior descending (LAD) coronary artery, extending the approach recently proposed to investigate the spatiotemporal evolution of intravascular flow patterns in the carotid artery to the analysis of **WSS** dynamics.[19] The use of CNs as a tool of analysis was motivated by their ability to synthetically and effectively characterize the structure and function of complex physical systems such as four-dimensional (4D) cardiovascular flows, as in the case object of the study. In fact, in the context of graph theory, CNs were used to model pairwise connections between highly interacting dynamical objects,[20,21] through a set of nodes and links. Recently, correlation-based CNs have been successfully applied to complex fluid mechanics phenomena.[22–25]

In detail, CNs were applied separately to WSS-based descriptors, measuring their spatiotemporal similarity by means of pairwise linear correlation between their time-histories along the cardiac cycle. Using a representative sample of computational hemodynamics models of pig coronary artery, CNs were applied to the time-histories of (1) **WSS** magnitude, and of three **WSS** multidirectionality descriptors,[11] namely (2) the "axial" **WSS** (aligned with the main flow direction), (3) the "secondary" **WSS** (orthogonal to the axial direction and related to secondary flows) and (4) the ratio between their magnitudes. The adopted network formalism and correlation strategy allowed the characterization of WSS time-histories from a new perspective, contributing to the knowledge of vascular wall dysfunction in coronary arteries, by providing a more in-depth insight into the multidirectional nature of **WSS**.

## Methods

### *Imaging and geometry reconstruction*

An overview of the methods is provided in Figure 1. The LAD of 10 ostensibly healthy adult Bretoncelles Meishan mini-pigs (age of $34 \pm 3$ months, castrated male) under general anesthesia was imaged by coronary computed tomography angiography (CCTA) and intravascular ultrasound (IVUS), as detailed elsewhere.[13,17] Doppler-based blood flow velocity measurements were acquired at several locations along each artery (i.e. at the inflow section and immediately upstream and downstream of each side branch) using the ComboWire (Volcano Corp., Rancho Cordova, CA, United States). For each vessel, the lumen contours were segmented from the IVUS images and stacked upon the three-dimensional (3D) CCTA centerline using MeVisLab (Bremen, Germany) (see De Nisco et al.,[13] for details). The 10 reconstructed luminal surfaces of the LADs are presented in the Supplementary Data (Figure S1). Further details about image acquisition and model reconstruction are described elsewhere.[13,17]

The study was conducted according to the National Institute of Health guide for the Care and Use of Laboratory animals.[26] Ethical approval was obtained to perform the study (EMC nr. 109-14-10).

### *Computational hemodynamics*

The finite volume method was applied to numerically solve the governing equations of fluid motion, that is, the Navier–Stokes equations, in their discrete form. To do that, the computational fluid dynamics (CFD) code Fluent (ANSYS Inc., Canonsburg, PA, United States) was used on discretized fluid domains of 6.5 million tetrahedrons on average (with curvature-based refinement and a five-layer prism at the lumen). Blood was assumed as an incompressible, homogeneous, non-Newtonian fluid.[27] Arterial walls were assumed to be rigid. Full details on the sensitivity of CFD results to grid refinement and on the adopted schemes are extensively reported in De Nisco et al.,[13] whereas the impact of the adopted assumptions on the rheological behavior of blood and on rigid walls has been extensively reported in previous studies.[28–31]

*In vivo* velocity ComboWire Doppler measurements were used to prescribe personalized boundary conditions, according to the previously proposed scheme.[13,17] Briefly, the most proximal measurement-based flow-rate value was applied at the inflow section in terms of time-dependent flat velocity profile. The measured flow split was estimated at each side branch based on the

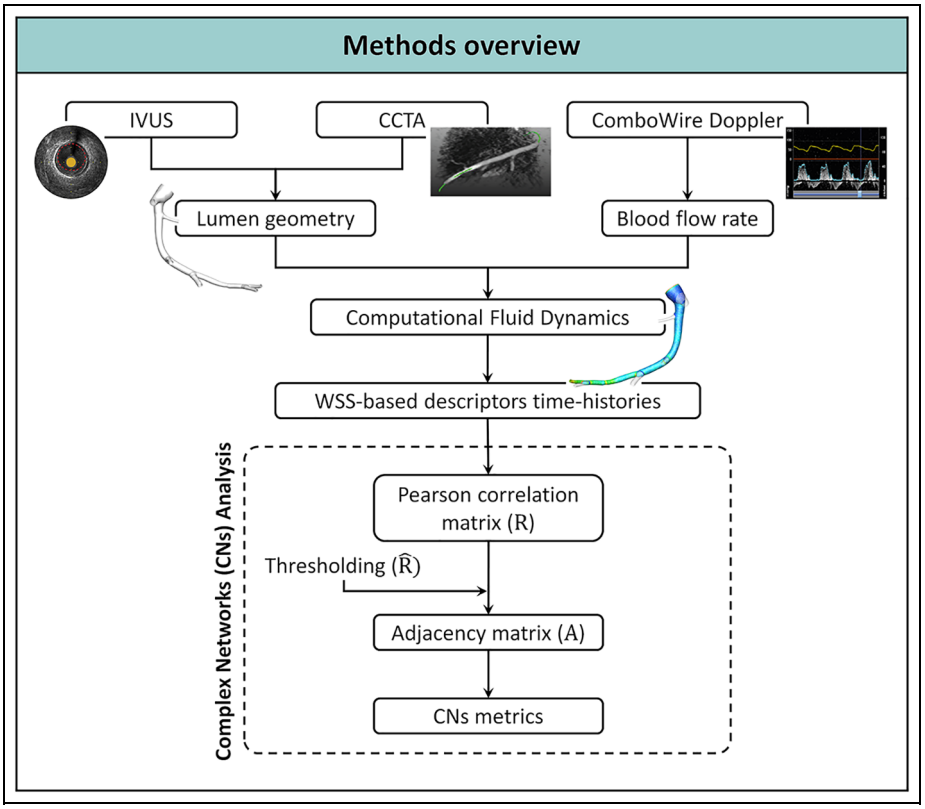


**Figure 1.** Schematic diagram of the study design, showing how imaging data contribute to define vessel geometry, hemodynamic variables and complex networks metrics.
CCTA: coronary computed tomography angiography; IVUS: intravascular ultrasound; WSS: wall shear stress; CNs: complex networks.

difference between upstream and downstream velocity-based flow-rate measurements and prescribed as outflow boundary. The Huo and Kassab[32] diameter-based scaling law was applied to estimate the flow ratio in those vessels where flow velocity measurements were inaccurate or not available. The no-slip condition was applied at wall boundaries. Here, data analysis was conducted on the main branch of LADs only, removing side branches in the post-processing step using the open-source Vascular Modeling Toolkit (VMTK, http://www.vmtk.org/).

## Hemodynamic descriptors

The analysis involved the hemodynamic descriptors listed in Figure 2. In detail, the instantaneous luminal distribution of **WSS** magnitude ($|\mathbf{WSS}|$) and of **WSS** multidirectionality descriptors was computed. Two projections of **WSS** were considered, respectively, along (1) the "axial" direction, identified by the tangent to the local vessel centerline ($\mathbf{WSS}_{ax}$) and related to the main flow direction, and (2) the "secondary" one, perpendicular to the local axial direction and related to secondary flows ($\mathbf{WSS}_{sc}$).[11] Moreover, to identify luminal regions where the local secondary component of **WSS** predominates over the axial one, the ratio of the secondary to axial **WSS** magnitude ($\mathrm{WSS}_{ratio}$) was evaluated. The cycle-average values of the investigated WSS-based hemodynamic descriptors were also computed and reported in Figure 2.

Regression analysis was conducted to investigate the relations among $|\mathbf{WSS}|$, $\mathbf{WSS}_{ax}$, $\mathbf{WSS}_{sc}$ and $\mathrm{WSS}_{ratio}$ time-histories along the cardiac cycle and reported as Pearson correlation coefficients. In detail, considering the time-histories along the cardiac cycle of the WSS-based quantities in each node of the wall surface mesh, for each LAD model, the following correlations were computed: (1) *"all-to-all"* correlations between time-histories at every pair of nodes $i$ and $j$ for each one of the WSS-based quantities defined above and denoted as: $\mathrm{R}_{i,j}^{|\mathrm{WSS}|}$, $\mathrm{R}_{i,j}^{ax}$, $\mathrm{R}_{i,j}^{sc}$ and $\mathrm{R}_{i,j}^{ratio}$; (2) *"layered"* correlations between time-histories of two different WSS-based quantities at the same node $i$, denoted as: $\mathrm{R}_{i}^{|\mathrm{WSS}|-ax}$ ($|\mathbf{WSS}|$ vs $\mathbf{WSS}_{ax}$ time-histories), $\mathrm{R}_{i}^{|\mathrm{WSS}|-sc}$ ($|\mathbf{WSS}|$ vs $\mathbf{WSS}_{sc}$ time-histories) and $\mathrm{R}_{i}^{ax-sc}$ ($\mathbf{WSS}_{ax}$ vs $\mathbf{WSS}_{sc}$ time-histories); (3) *"one-to-all"* correlations between the personalized inlet flow-rate Q and the $|\mathbf{WSS}|$, $\mathbf{WSS}_{ax}$ and $\mathbf{WSS}_{sc}$ time-history at each node $i$, denoted, respectively, as $\mathrm{R}_{i}^{\mathrm{Q}-|\mathrm{WSS}|}$, $\mathrm{R}_{i}^{\mathrm{Q}-ax}$ and $\mathrm{R}_{i}^{\mathrm{Q}-sc}$. Explanatory examples of pairs of nodal time-histories with different correlation strength and sign are presented in Figure 2.

## CNs: definitions and construction

In graph theory, a network is defined by a set $V$ of $N$ nodes connected by a set $E$ of links (Figure 2). In an *undirected* network, each link is an unordered pair of nodes $i$ and $j$, and is denoted as $\{i, j\}$. In this study, we analyzed *spatial networks*, that is, networks where

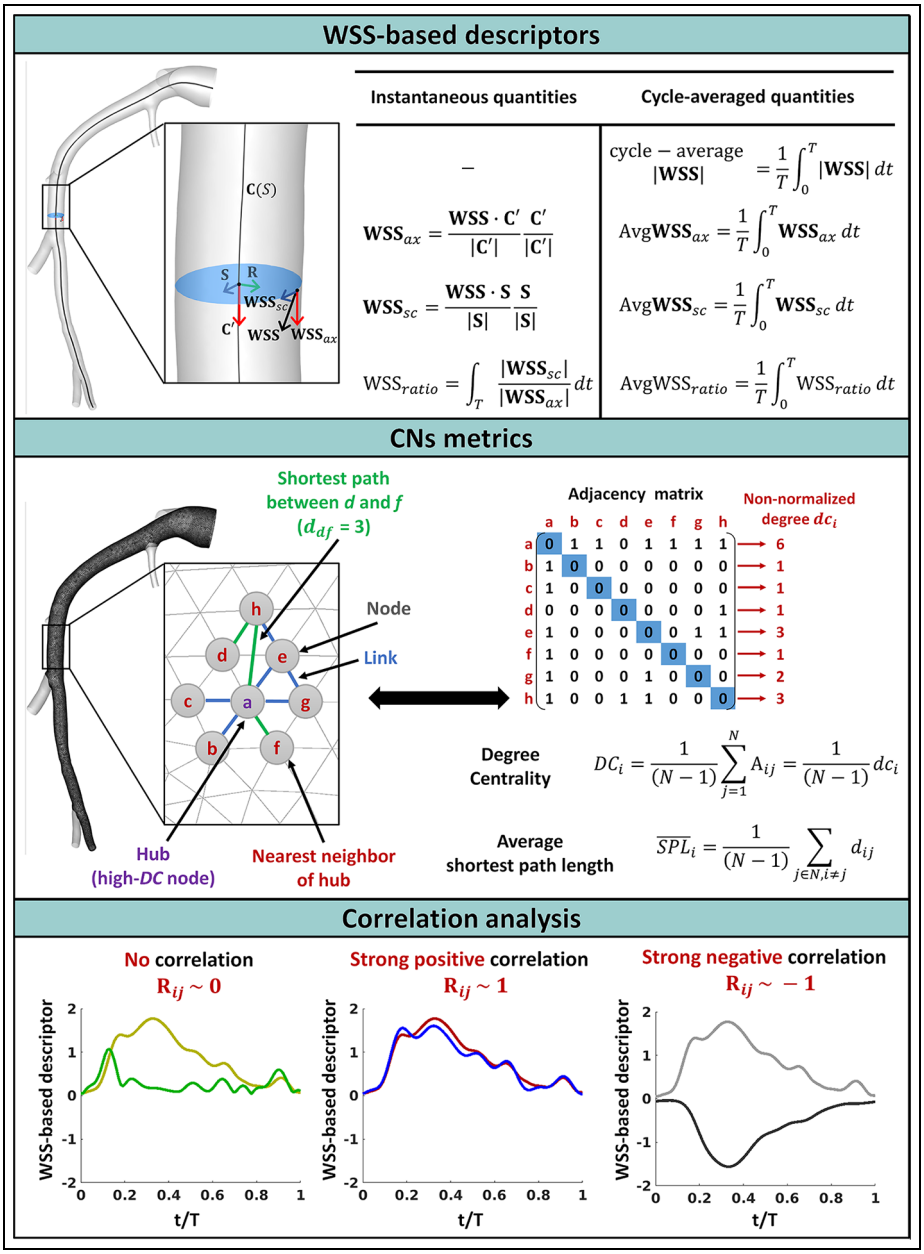


**Figure 2.** Methodology of hemodynamic descriptors, complex networks metrics and correlation assessment and analysis. WSS-based descriptors panel: example of **WSS** vector acting in a generic point at the luminal surface. Its axial ($\mathbf{WSS}_{ax}$) and secondary ($\mathbf{WSS}_{sc}$) components are also displayed. Instantaneous and cycle-average $\mathbf{WSS}_{ax}$, $\mathbf{WSS}_{sc}$ and $WSS_{ratio}$ mathematical definitions are reported. C(*S*): vessel centerline; $\mathbf{C}'$: vector tangent to the centerline; **R**: vector perpendicular to $\mathbf{C}'$ directed from the centerline to the generic point at the arterial surface; **S**: vector orthogonal to vectors **R** and $\mathbf{C}'$; *T*: period of the cardiac cycle. CNs metrics panel: explanatory example of a CN with its nodes and links, and the corresponding adjacency matrix. CNs metrics *DC* and $\overline{SPL}$ mathematical definitions are reported. *N*: number of nodes; $dc_i$: non-normalized degree centrality of node *i*; $d_{ij}$: shortest topological distance between nodes *i* and *j*. Correlation analysis panel: explanatory examples of differently correlated pairs of WSS-based descriptors time-histories along the cardiac cycle of duration *T*, as defined by the $R_{ij}$ correlation coefficients.

nodes occupy a fixed position in the Euclidean space, here represented by the nodes of the surface elements of the mesh grid lying on the luminal surface.

In each LAD coronary model, CNs were constructed as follows. First, the Pearson correlation coefficients $R_{ij}$ between time-histories along the cardiac cycle of each considered WSS-based quantity in generic nodes *i* and *j* were calculated. Then, CNs were built by applying a correlation criterion[19]: if the correlation coefficient $R_{ij}$ is larger than a given threshold $\hat{R}$, the nodes *i* and *j* are considered connected and a topological link $\{i, j\}$ between them is built. The median value of the overall distribution obtained by pooling together the $R_{ij}$ correlation coefficients of all 10 LAD models was set as threshold $\hat{R}$ to build the CN for each WSS-based quantity. Threshold values were used to convert each correlation matrix in an *adjacency matrix* for each CN, according to the criterion

$$A_{ij} = \begin{cases} 0, & if\ \{i,j\} \notin E\ or\ i = j \\ 1, & if\ \{i,j\} \in E \end{cases} \quad (1)$$

where $E$ is the set of the CN links. Matrix A contains all the information about node connectivity: $A_{ij} = 1$ if a link exists between nodes $i$ and $j$ (i.e. if $R_{ij} > \hat{R}$) and is equal to zero otherwise (Figure 2). In this study, matrix A is symmetric ($A_{ij} = A_{ji}$) and the *undirected* CNs were constructed following the steps in Figure 1.

### CNs metrics

Two topological CNs metrics were used to characterize the structure of the networks (Figure 2). The first one is the *degree centrality* ($DC_i$), a measure of the centrality of a node inside the network. $DC_i$ is defined as the percentage of nodes of the network directly connected to node $i$, that is, the so-called *nearest neighborhood* of $i$. Here, $DC_i$ is normalized over the total number $(N-1)$ of possible neighbors of $i$

$$DC_i = \frac{1}{(N-1)} \sum_{j=1}^{N} A_{ij} = \frac{1}{(N-1)} dc_i \quad (2)$$

where $dc_i$ is the non-normalized degree centrality of node $i$. The normalization in equation (2) allows comparisons between networks of different number of nodes ($N$). In synthesis, $DC_i$ quantifies the relative number of neighbors (i.e. directly connected nodes) a node has in the network or, in other words, the fraction of time-histories of a specific WSS-based quantity, correlated above threshold with the time-history in node $i$.

The second CNs metric used in this study allows the quantification of the topological "persistence length" of correlation of **WSS** spatiotemporal patterns. It is a measure of the topological distance between one node and the rest of the nodes in the network, and it is called *average shortest path length* ($\overline{SPL_i}$) of node $i$

$$\overline{SPL_i} = \frac{1}{(N-1)} \sum_{j \in N, i \neq j} d_{ij} \quad (3)$$

$\overline{SPL_i}$ is defined as the mean of the *shortest path lengths* from node $i$ to every other node in the network, where $d_{ij} \in \mathbb{Z}$ is the shortest topological distance between nodes $i$ and $j$, that is, the minimum number of links that have to be crossed from node $i$ to node $j$[20] (Figure 2). By definition, if nodes $i$ and $j$ are connected, $d_{ij}$ equals 1 as there is one direct link between them, otherwise $d_{ij} > 1$. Roughly speaking, in a "fully" connected network all the nodes present direct links and $\overline{SPL_i}$ is equal to 1 in each node $i = 1, ..., N$. If there are no paths between node $i$ and the rest of the network, $\overline{SPL_i}$ is equal to infinity by definition.

To summarize, in the CNs-based characterization of **WSS** spatiotemporal heterogeneity, metrics $DC$ and $\overline{SPL}$ allow, respectively, the identification/visualization of spatial region where the **WSS** features are the most representative of the whole network, and the measurement of their topological "sphere of influence" through the quantification of their network persistence length of the correlation.

## Results

### "All-to-all" correlations of time-varying WSS-based descriptors

The luminal distributions of all the cycle-average WSS-based hemodynamic descriptors considered here (denoted as cycle-average $|\mathbf{WSS}|$, Avg$\mathbf{WSS}_{ax}$, Avg$\mathbf{WSS}_{sc}$ and Avg$WSS_{ratio}$) are reported in Figure 3 and Figure S2 (Supplementary Data).

The probability density function (PDF) of the correlations between the WSS-based quantities nodal time-histories is presented in Figure 4 for each investigated case. It emerges that the dynamics of $|\mathbf{WSS}|$ signals, as well as $\mathbf{WSS}_{ax}$, are always strongly correlated (as clearly evident by the markedly left-skewed shape of the PDFs in Figure 4, top panels). Moreover, the intra-model correlation distributions of $|\mathbf{WSS}|$ and $\mathbf{WSS}_{ax}$ quantities are almost coincident, as also proven by their median values (Table 1).

Those results imply that the **WSS** vector is markedly aligned with the axial direction (i.e. the main flow direction) along the cardiac cycle (Figure S3 in the Supplementary Data), in agreement with cycle-average $|\mathbf{WSS}|$ and Avg$\mathbf{WSS}_{ax}$ luminal distributions presented in Figure 3 (top and mid panels). On the other hand, in each coronary model under study, the correlation distribution of $\mathbf{WSS}_{sc}$ time-histories exhibits a bimodal shape (Figure 4, bottom-left panel), with the two peaks located close to the extreme values of the correlation range ($R_{ij}^{sc} = -1$ and $R_{ij}^{sc} = 1$). Such a kind of $R_{ij}^{sc}$ distributions highlights that in the LAD (1) $\mathbf{WSS}_{sc}$ time-histories are either markedly positively or negatively correlated, and that (2) this is an emergent feature of LAD hemodynamics. The emerged existence of both strong correlations and anti-correlations between $\mathbf{WSS}_{sc}$ time-histories is reflected in the presence of two distinct, opposite oriented Avg$\mathbf{WSS}_{sc}$ vectors at the luminal surface of the vessels (Figure 3, bottom panel), since the opposite signs of instantaneous $\mathbf{WSS}_{sc}$ values highlight "out-of-phase," that is, opposite vectors direction (Figure 2).

Notably, although $\mathbf{WSS}_{ax}$ and $\mathbf{WSS}_{sc}$ correlation distributions have the same shape for all the investigated cases (left-skewed and bimodal, respectively), a larger inter-variability characterizes the correlation distributions of $WSS_{ratio}$ time-histories (Figure 4, bottom-right panel). In particular, while some of the LAD models present an almost flat distribution of $R_{ij}^{ratio}$ values, the other ones exhibit a PDF with a peak centered around the zero correlation value, or close to the value $R_{ij}^{ratio} = 1$. Coronary models characterized by a higher probability of uncorrelated $WSS_{ratio}$ time-histories (i.e. models A, D, H and I, with a PDF peak around $R_{ij}^{ratio} = 0$, Figure 4, bottom-right panel) exhibit a less uniform distribution of Avg$WSS_{ratio}$ at the luminal

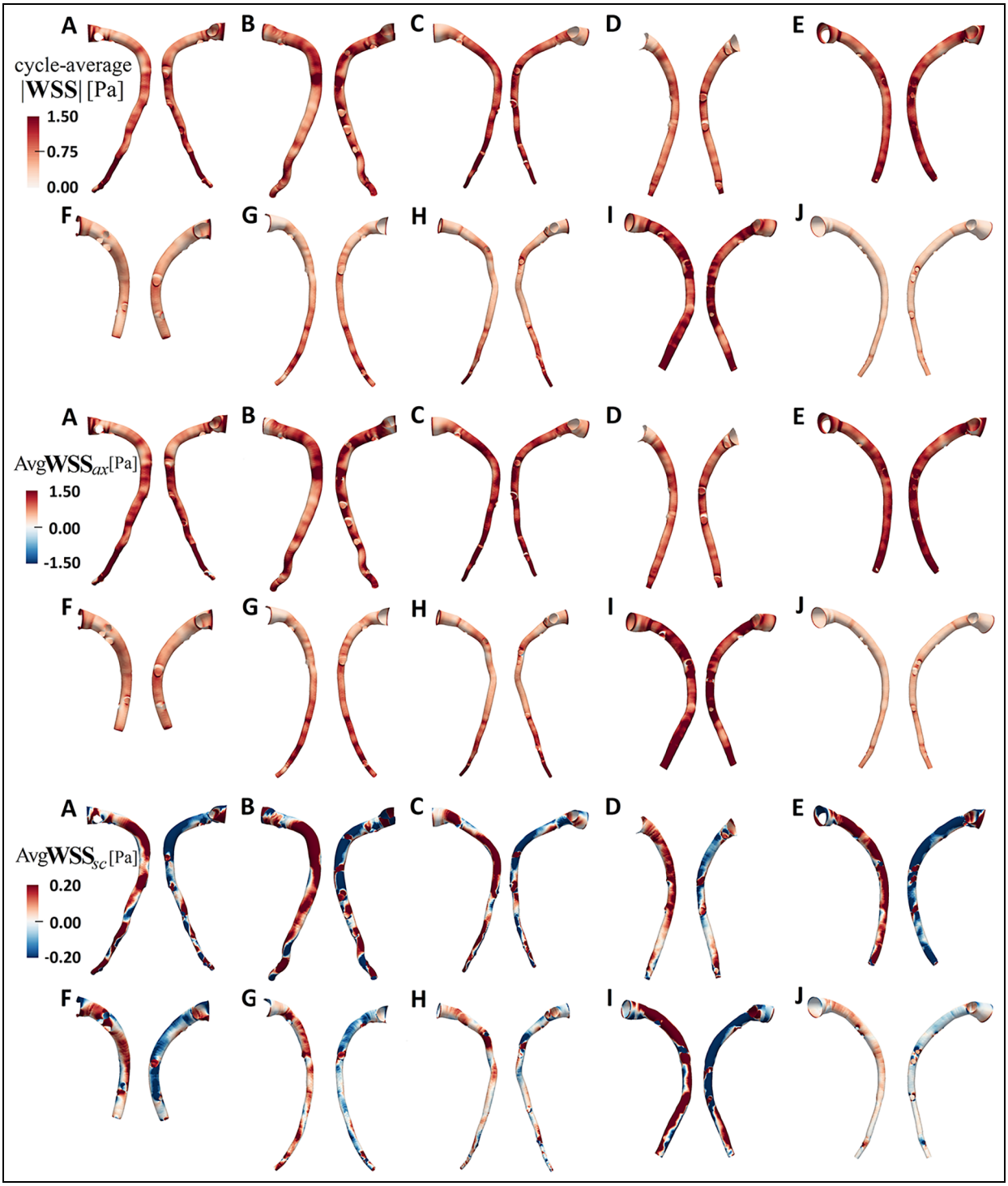


**Figure 3.** Luminal surface distributions of cardiac cycle-average **WSS** vector magnitude (top panel) and its axial and secondary projections (Avg**WSS**$_{ax}$, mid panel; Avg**WSS**$_{sc}$, bottom panel), for all the LAD models. For Avg**WSS**$_{ax}$, colors identify the forward (red) and backward (blue) flow direction. Cycle-average |**WSS**| and Avg**WSS**$_{ax}$ luminal distributions are very similar, suggesting the major contribution of **WSS**$_{ax}$ to the overall **WSS** vector. For Avg**WSS**$_{sc}$, colors identify the right (red) and left-handed (blue) direction. Avg**WSS**$_{sc}$ visualization range was properly narrowed to highlight **WSS**$_{sc}$ directionality.

surface (Figure S2, Supplementary Data), with extended regions of AvgWSS$_{ratio} \geqslant 1$. This observation suggests that the presence of uncorrelated waveforms is localized in those regions at the luminal surface where **WSS** secondary component predominates over (or, at most, equals) the axial one. This interpretation of the observed results is also corroborated by the fact that the LAD model with a peak on $R_{ij}^{ratio} = 1$ (model E) is the one characterized by the most uniform distribution of AvgWSS$_{ratio}$ (mostly $< 1$), with **WSS** axial component on the main branch predominating over the secondary component.

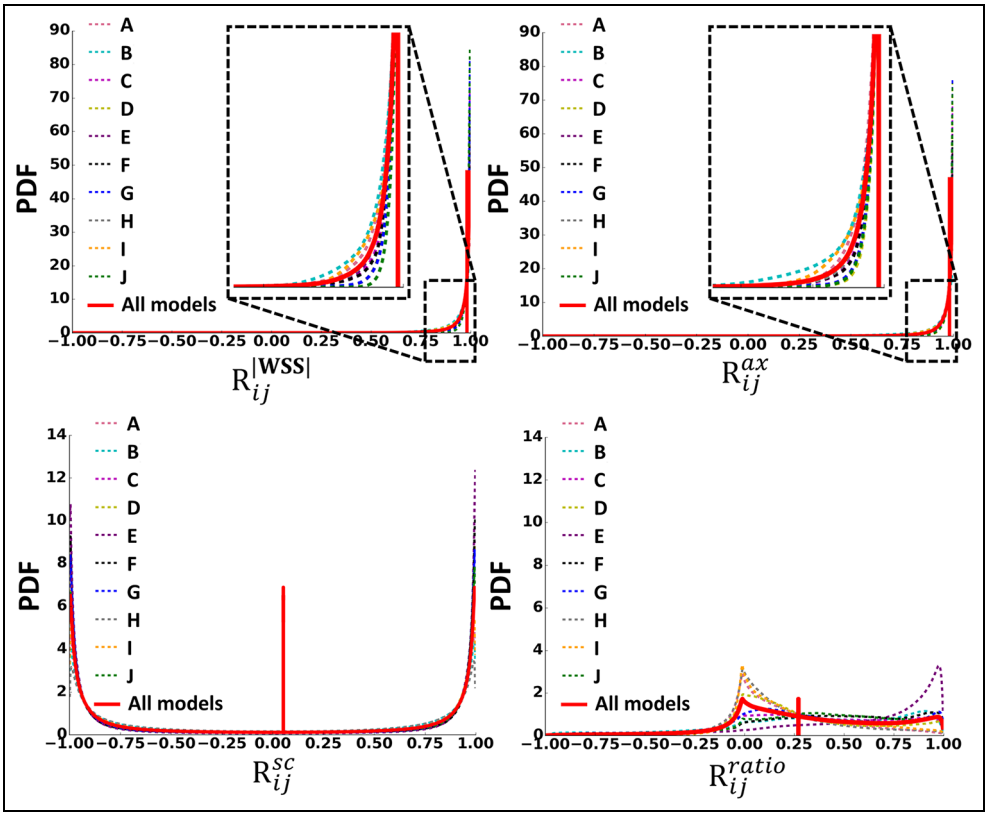


**Figure 4.** Probability density functions (PDFs) of the correlation coefficients: $R_{ij}^{|WSS|}$ (top-left), $R_{ij}^{ax}$ (top-right), $R_{ij}^{sc}$ (bottom-left) and $R_{ij}^{ratio}$ (bottom-right), in the *"all-to-all"* analysis $R_{ij}^{|WSS|}$ and $R_{ij}^{ax}$ PDFs show that the dynamics of $|\mathbf{WSS}|$ signals, as well as $\mathbf{WSS}_{ax}$, are strongly correlated (markedly left-skewed shape), and almost coincident. This implies that the **WSS** vector is predominantly aligned with the axial forward flow direction. $R_{ij}^{sc}$ PDFs exhibit a bimodal shape highlighting that $\mathbf{WSS}_{sc}$ time-histories are either markedly positively or negatively correlated. A larger inter-variability characterizes $R_{ij}^{ratio}$ correlation distributions: while some of the models present an almost flat distribution, the other ones exhibit a PDF with a peak centered around the zero correlation value, or close to the value $R_{ij}^{ratio} = 1$. The median value from all 10 models was set as threshold $\hat{R}$ to build the CN for each WSS-based quantity.

**Table 1.** Median values of $R_{ij}$ coefficients of the *"all-to-all"* correlation analysis.

| LAD model | $R_{ij}$ median values | | | |
|---|---|---|---|---|
| | $R_{ij}^{\|WSS\|}$ | $R_{ij}^{ax}$ | $R_{ij}^{sc}$ | $R_{ij}^{ratio}$ |
| A | 0.972 | 0.970 | 0.008 | 0.141 |
| B | 0.963 | 0.953 | 0.107 | 0.388 |
| C | 0.988 | 0.986 | 0.089 | 0.341 |
| D | 0.989 | 0.990 | 0.287 | 0.204 |
| E | 0.985 | 0.982 | 0.043 | 0.702 |
| F | 0.987 | 0.984 | 0.019 | 0.445 |
| G | 0.990 | 0.989 | 0.025 | 0.289 |
| H | 0.978 | 0.981 | 0.043 | 0.116 |
| I | 0.974 | 0.970 | 0.009 | 0.160 |
| J | 0.992 | 0.990 | 0.064 | 0.407 |
| All models | 0.982 | 0.982 | 0.054 | 0.270 |

LAD: left anterior descending.

## *"Layered" correlations of time-varying WSS-based descriptors*

On each LAD model, *"layered"* correlations were computed to measure the dynamical similarity between different WSS-based descriptors at the same node of the superficial mesh. The contour map of $R_i^{ax-sc}$ ($\mathbf{WSS}_{ax}$ vs $\mathbf{WSS}_{sc}$) values at the luminal surface is displayed in Figure 5, and the $R_i^{|WSS|-ax}$ ($|\mathbf{WSS}|$ vs $\mathbf{WSS}_{ax}$) and $R_i^{|WSS|-sc}$ ($|\mathbf{WSS}|$ vs $\mathbf{WSS}_{sc}$) contour maps are presented in the Supplementary Data (Figure S4).

As already emerged qualitatively from the PDFs (Figure 4, top panels) from previous results, the quantitative *"layered"* analysis confirms that the dynamics of $|\mathbf{WSS}|$ and $\mathbf{WSS}_{ax}$ time-histories in each node are strongly correlated ($>0.90$, Figure S4 top panel, in the Supplementary Data) in each LAD model. This spatio-temporal similarity in $|\mathbf{WSS}|$ and $\mathbf{WSS}_{ax}$ time-histories cannot emerge from the analysis of cycle-average $|\mathbf{WSS}|$ and $\mathrm{Avg}\mathbf{WSS}_{ax}$ luminal surface distributions (Figure 3, top and mid panels), which does not furnish any information about WSS waveforms dynamics. Consequently, comparing $\mathbf{WSS}_{sc}$ with $|\mathbf{WSS}|$ or $\mathbf{WSS}_{ax}$ time-histories gives almost identical distributions of $R_i^{|WSS|-sc}$ and $R_i^{ax-sc}$ (Figure S4 bottom panel and Figure 5, respectively). Correlation patterns at the luminal surface are markedly affected by the $\mathbf{WSS}_{sc}$ directionality ($R_i^{|WSS|-sc}$ and $R_i^{ax-sc}$ maps recall the patterns of $\mathrm{Avg}\mathbf{WSS}_{sc}$ (Figure 3 bottom panel)), although

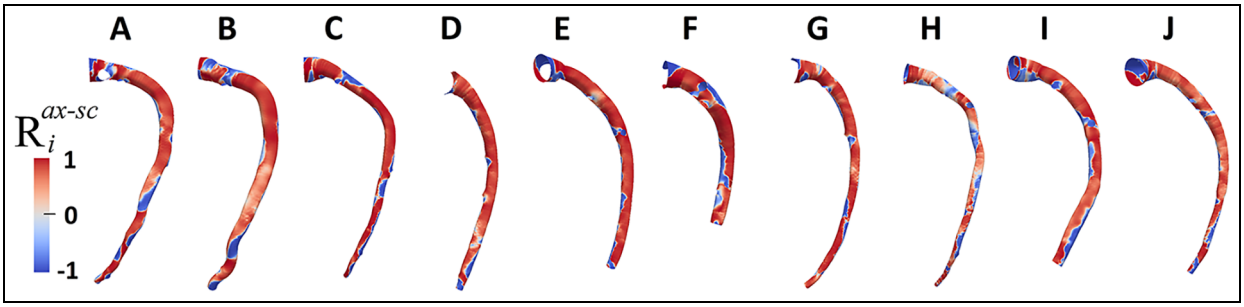


**Figure 5.** Luminal surface contour maps of "*layered*" correlation $R_i^{ax-sc}$ between axial ($\mathbf{WSS}_{ax}$) and secondary ($\mathbf{WSS}_{sc}$) projections of **WSS** vector at the same node *i* of the superficial mesh, for all the investigated LAD models. $\mathbf{WSS}_{ax}$ versus $\mathbf{WSS}_{sc}$ correlation patterns at the luminal surface are markedly affected by $\mathbf{WSS}_{sc}$ directionality ($R_i^{ax-sc}$ maps recall the patterns of Avg$\mathbf{WSS}_{sc}$, see bottom panel of Figure 3). Luminal surface areas with negative (positive) $R_i^{ax-sc}$ values are regions where the secondary and the axial **WSS** are "out of phase" ("in phase").

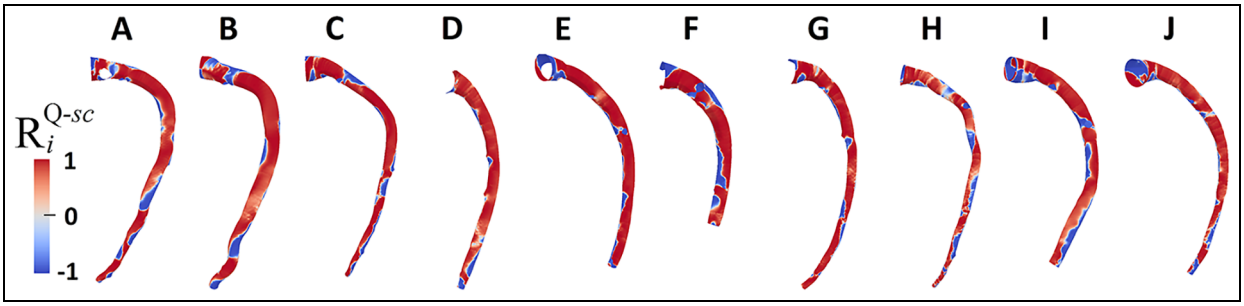


**Figure 6.** Luminal surface contour maps of "*one-to-all*" correlation $R_i^{Q-sc}$ between pig-specific LAD inlet flow-rate (Q) waveform and secondary projection of **WSS** vector ($\mathbf{WSS}_{sc}$) at the generic node *i* of the superficial mesh, for all the investigated LAD models. $R_i^{Q-sc}$ is markedly affected by $\mathbf{WSS}_{sc}$ directionality, recalling Avg$\mathbf{WSS}_{sc}$ patterns at the luminal surface (see bottom panel of Figure 3). Luminal surface areas with negative $R_i^{Q-sc}$ values are regions subjected to $\mathbf{WSS}_{sc}$ "out of phase" with the inlet flow-rate.

its contribution to the **WSS** vector is overall poor, compared to $\mathbf{WSS}_{ax}$. This is because, by definition, the correlation is a measure of similarity between the shape of the time-histories, and not their amplitude. Therefore, when considering **WSS** predominantly aligned with the positive axial direction, positive/negative (i.e. right-/left-handed) $\mathbf{WSS}_{sc}$ time-histories result in positive/negative *"layered"* $R_i^{|WSS|-sc}$ and $R_i^{ax-sc}$ correlations. In the latter case, this is like saying that the consequence for the hemodynamics establishing in the LAD is that there are regions of the luminal surface where the secondary and the axial **WSS** are "in phase" or "out-of-phase" (Figure 5).

### *"One-to-all" correlations: inlet flow-rate versus WSS-based descriptors*

The *"one-to-all"* correlation approach was implemented to measure the statistical interdependence between the pig-specific LAD inlet flow-rate Q and the WSS-based descriptors time-histories in each node *i*. The *"one-to-all"* correlation maps (Figure S5, Supplementary Data) highlight a uniform distribution of strong positive correlation values both for Q versus |**WSS**| and Q versus $\mathbf{WSS}_{ax}$ time-histories, in all LAD models. In the absence of regions of marked flow recirculation or separation, and with the Q time-history in the investigated LAD arteries always indicating forward blood inflow, we can conclude that the shape of the inlet flow-rate waveform "propagates" along the vessel strongly conditioning both |**WSS**| and $\mathbf{WSS}_{ax}$ time-histories. On the contrary, Q versus $\mathbf{WSS}_{sc}$ time-histories correlation distributions reflect, as observed for $R_i^{|WSS|-sc}$ and $R_i^{ax-sc}$ maps (Figure S4 bottom panel, Supplementary Data and Figure 5), the signed (right- and left-handed orientation) distribution of $\mathbf{WSS}_{sc}$ at the luminal surface, leading to a succession of high positive and high negative $R_i^{Q-sc}$ regions (Figure 6). This is like saying that the presence of luminal regions subjected to a secondary **WSS** "out-of-phase" with the inlet flow-rate clearly emerges.

### *CNs*

Based on the median values of the overall PDFs distribution obtained by pooling together the $R_{ij}$ of all the 10 LAD models for each WSS-based quantity (Figure 4), the following threshold values were obtained: $\hat{R}^{|WSS|} = 0.982$, $\hat{R}^{ax} = 0.982$, $\hat{R}^{sc} = 0.054$ and $\hat{R}^{ratio} = 0.270$ and used to build the |**WSS**|, $\mathbf{WSS}_{ax}$,

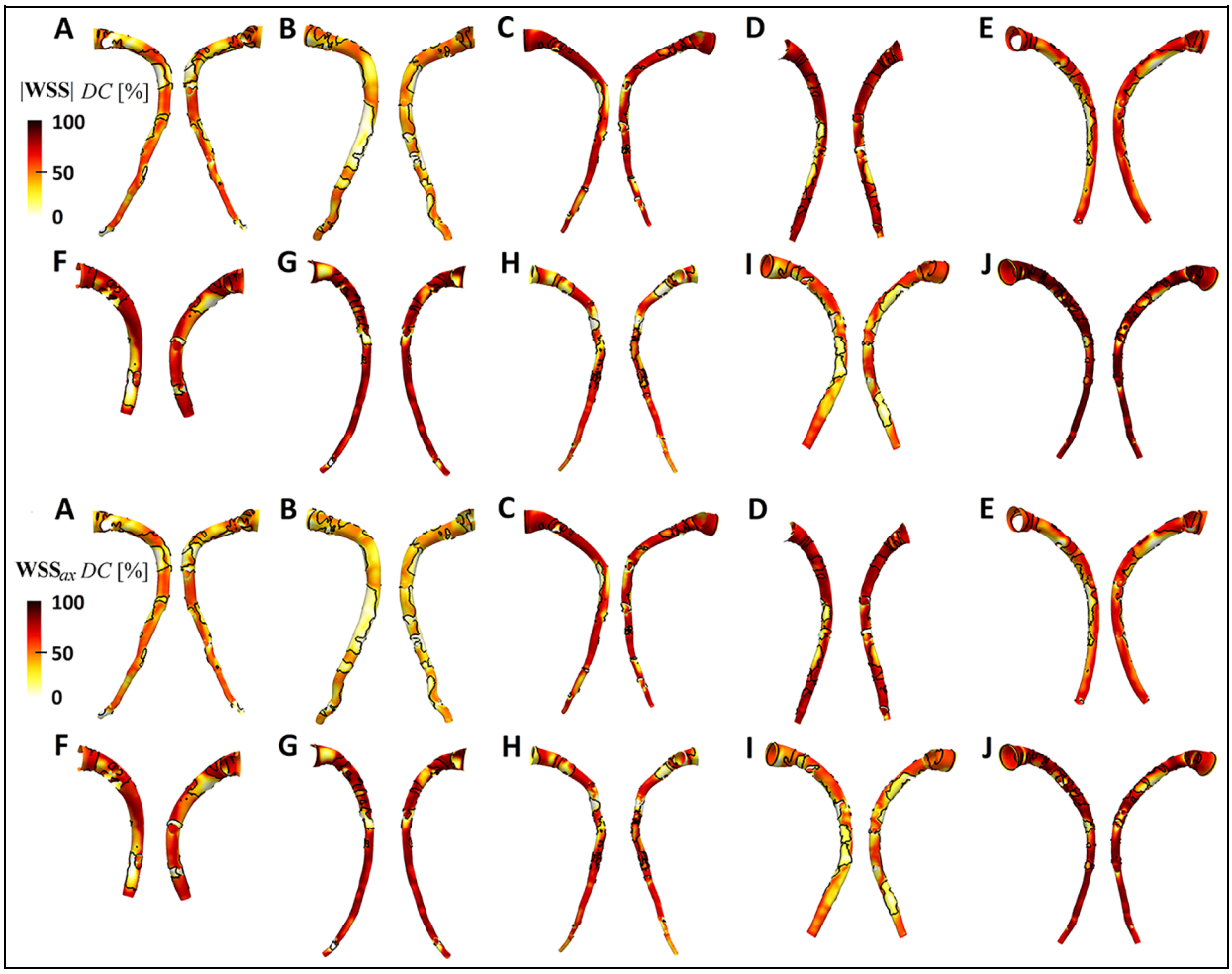


**Figure 7.** Luminal distributions of normalized degree centrality (*DC*) for the 10 |**WSS**| (top panel) and $\mathbf{WSS}_{ax}$ (bottom panel) CNs. |**WSS**| and $\mathbf{WSS}_{ax}$ have almost identical topologies, with the more topologically isolated regions (low *DC*) preferentially located at the inner wall of all LAD models. These regions co-localize with luminal surface areas exposed to low cycle-average |**WSS**|, here displayed by the black contour lines representing the artery-specific lower cycle-average |**WSS**| tertile.

$\mathbf{WSS}_{sc}$ and $\mathrm{WSS}_{ratio}$ networks, respectively. The analysis of the luminal distributions of the normalized *DC* (Figure 7) shows that |**WSS**| and $\mathbf{WSS}_{ax}$ CNs have almost identical topologies. In particular, in both networks, the more topologically isolated (low *DC*) regions are preferentially located at the inner wall (e.g. see models D, E, F and J), where the nearest neighborhoods of |**WSS**| and $\mathbf{WSS}_{ax}$ time-histories are a small fraction ($DC < 15\%$) of the network nodes. Interestingly, such low *DC* regions co-localize very well with the luminal surface areas exposed to low cycle-average |**WSS**| (Figure 7). The *DC* maps of the $\mathbf{WSS}_{sc}$ (Figure 8) reflect the presence of opposite-signed secondary components characterizing **WSS** multidirectionality. In fact, $\mathbf{WSS}_{sc}$ time-histories correlated beyond the set threshold form two main separated regions of different *DC*. This is clearly evident in only some of the models in Figure 8, that is, models B, C, D, H and J, because of the common scale set for *DC* maps visualization. Narrowing the visualization range, the two separated *DC* regions can be clearly identified also in the rest of the models, as in Figure S6 of the Supplementary Data.

The quantitative information provided by the *DC* metric proves that in two large portions (in general around 35% and 65%) of the LAD wall the secondary **WSS** exhibits very similar time-dependent behaviors, despite its modest contribution to the overall **WSS** dynamics (Figure 8). The visual inspection of the *DC* luminal distributions of the $\mathrm{WSS}_{ratio}$ (Figure 9) highlights that some of the LAD models (A, D, H and I) present lower *DC* values than the other ones. This is the consequence of their $\mathrm{R}_{ij}^{ratio}$ distributions (Figure 4, bottom-right), characterized by the highest probability of uncorrelated $\mathrm{WSS}_{ratio}$ time-histories. On the opposite, LAD model E, characterized by a PDF with a peak close to $\mathrm{R}_{ij}^{ratio} = 1$, presents a markedly connected network, with an almost uniform *DC* distribution above 75% (Figure 9). Notably, as observed for |**WSS**| and $\mathbf{WSS}_{ax}$, also for the $\mathrm{WSS}_{ratio}$-based CN low *DC* areas co-localize with the luminal surface area subjected to low cycle-average |**WSS**| (Figure 9).

The visualization of the $\overline{SPL}$ luminal distributions for the 10 LAD models here considered is available in Figures S7 and S8 of the Supplementary Data. In

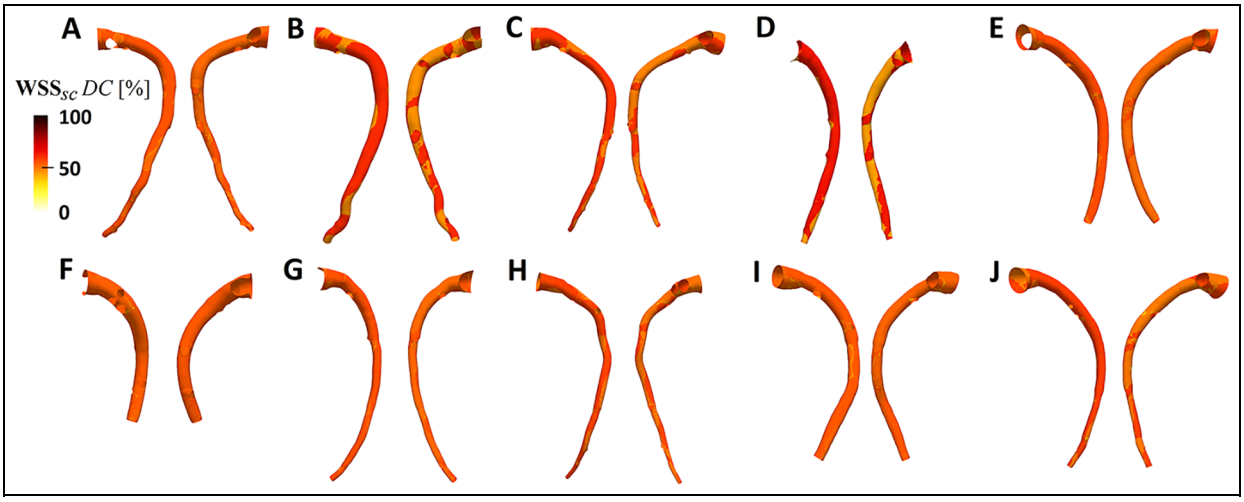


**Figure 8.** Luminal distributions of normalized degree centrality (*DC*) for the 10 **WSS**$_{sc}$ CNs. The *DC* maps reflect the presence of opposite-signed secondary components characterizing **WSS**$_{sc}$ directionality (see bottom panel of Figure 3). Two main separated regions of different *DC* emerge, indicating **WSS**$_{sc}$ time-histories correlated beyond the set threshold (see also Figure S6 of the Supplementary Data).

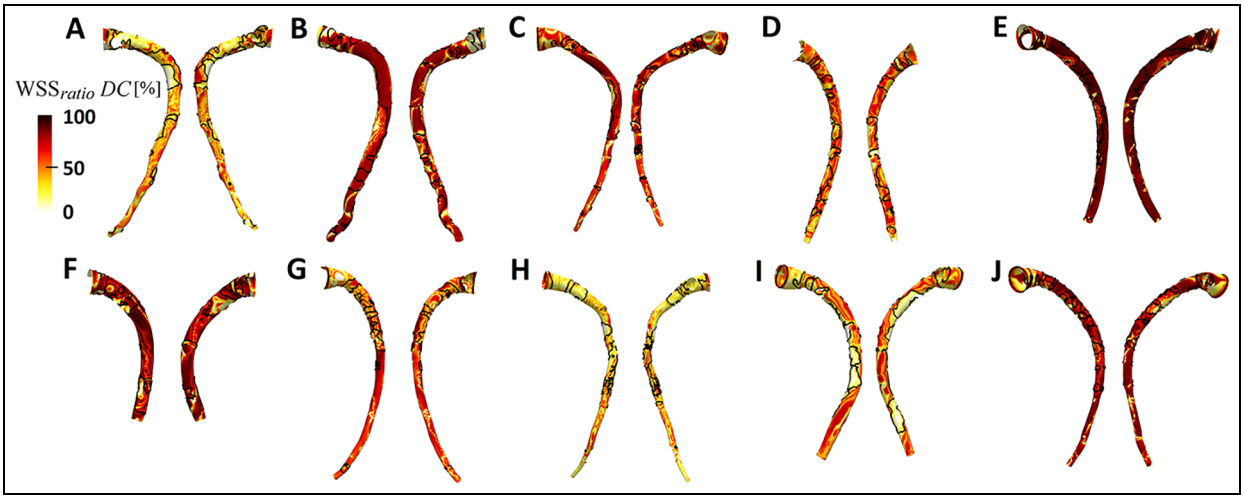


**Figure 9.** Luminal distributions of normalized degree centrality (*DC*) for the 10 WSS$_{ratio}$ CNs. Low *DC* areas co-localize with the luminal surface area subjected to low cycle-average |**WSS**|, here displayed by the black contour lines representing the artery-specific lower |**WSS**| tertile.

Figure 10, the $\overline{SPL}$ luminal distributions are presented for two explanatory LAD models (B and H). The $\overline{SPL}$ is a measure of the topological "persistence length" of correlations, in particular, the shorter the topological distance between each nodal time-history and the rest of the network, the longer the correlation persistence length. As a first observation common to all the LAD models, we report that |**WSS**|- and **WSS**$_{ax}$-based networks present similar $\overline{SPL}$ distributions at the luminal surface, although some of the **WSS**$_{ax}$ CNs are more disperse than the corresponding |**WSS**| ones (this is the case of, for example, model B in Figure 10, where $\overline{SPL}$ is higher for the **WSS**$_{ax}$ networks). In each LAD model, nodes with a markedly different |**WSS**| and **WSS**$_{ax}$ dynamic behavior are topologically separated from the rest of the nodes on the luminal surface by 2.25 links, at least. These regions co-localize with areas at the luminal surface exposed to low cycle-average |**WSS**| (Figure 10, and Figure S7 of the Supplementary Data). Regarding the $\overline{SPL}$ maps of the **WSS**$_{sc}$ network, these are characterized by a less pronounced inter-variability, with shorter topological paths (around 1.5 links-long on average, Figure 10, and Figure S8 of the Supplementary Data) separating nodal time-histories and, subsequently, a stronger persistence of the spatiotemporal correlations. This overall uniform $\overline{SPL}$ distributions confirm the dynamical similarity characterizing the **WSS**$_{sc}$ in the investigated dataset, as suggested also by the *DC* analysis. Finally, the $\overline{SPL}$ luminal distributions of the WSS$_{ratio}$-based networks present topologically isolated regions co-localized with luminal

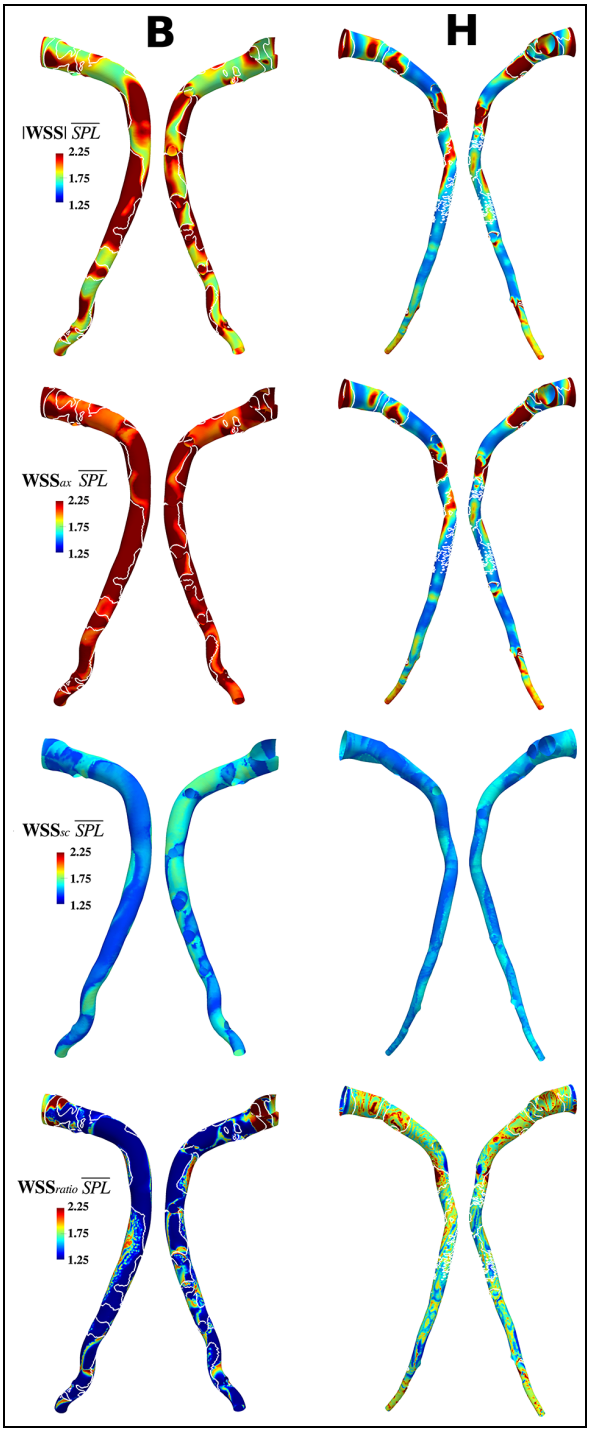


**Figure 10.** Luminal distributions of *average shortest path length* ($\overline{SPL}$) of |**WSS**| and WSS-based descriptors (**WSS**$_{ax}$, **WSS**$_{sc}$ and WSS$_{ratio}$) CNs, for two explanatory LAD models (B and H). The white contour lines represent the artery-specific lower cycle-average |**WSS**| tertile. |**WSS**|- and **WSS**$_{ax}$-based networks present similar $\overline{SPL}$ luminal distributions, although for case B the **WSS**$_{ax}$ CN is more disperse than the |**WSS**| ones. In each LAD model, nodes with higher |**WSS**| and **WSS**$_{ax}$ $\overline{SPL}$ co-localize with areas exposed to low cycle-average |**WSS**|. The $\overline{SPL}$ maps of the **WSS**$_{sc}$ CN show shorter topological paths, indicating a stronger persistence of the spatiotemporal correlations. The $\overline{SPL}$ maps of the WSS$_{ratio}$ networks present topologically isolated regions (identified by higher $\overline{SPL}$ values) co-localized with luminal surface areas exposed to low cycle-average |**WSS**|.

surface areas exposed to low cycle-average |**WSS**|, such as for models B and H in Figure 10.

## Discussion

The reported association of low **WSS** magnitude with increased inflammation and lipid content supports the hypothesis that such hemodynamic feature plays a relevant role in plaque initiation in coronary arteries.[33] More recent findings provide additional insight to the low WSS hypothesis, reporting associations observed between low WSS and plaque morphology and composition (see, for example, Gijsen et al.[34]). In addition, in a very recent study, it is reported that low WSS incrementally improves the positive predictive values for the development of plaque.[35] However, parallel to the identification of an established active role for low WSS in the onset and progression of the atherosclerotic disease, recent studies reported that there is a weak association between lesions localization and low/oscillatory **WSS**.[5–8] This indicates the needs for a broader study of **WSS** features to deepen the knowledge on the relationship between the complex hemodynamic milieu and coronary vessels biology. Most of the studies on the role of WSS in the development of atherosclerosis apply a "reductionist" mathematical approach based on cycle-averaged quantities. Such approach, mostly justified by the clinical need of synthetizing the information of 4D data, neglects the relevance of **WSS** spatiotemporal evolution, especially when clearly recognizable correlated patterns can be observed. To contribute to fill this gap of knowledge, in this study, the **WSS** spatiotemporal heterogeneity in coronary arteries is investigated through a correlation-based and a CNs approach. The new perspective offered by network science allows the identification of correlated **WSS** patterns, by drawing upon the similarity between their dynamical behaviors encoded in the time-histories that are associated to the nodes of the networks. The findings of this study are summarized in Table 2.

The combined results of the correlation analysis presented here provide, for the first time, a quantitative proof of the fact that **WSS** in the investigated LAD models is, overall, unidirectional and aligned with the forward flow direction (Figure S3 in the Supplementary Data). Moreover, from the *"one-to-all"* analysis it emerges that, in the absence of regions of marked flow separation and/or recirculation, the flow-rate waveform at the inflow of the LAD shapes both the |**WSS**| and **WSS**$_{ax}$ time-histories. This result demonstrates, for the first time, the impact of the inlet flow-rate in shaping **WSS** patterns on the LAD artery luminal wall. The strong influence of Q on WSS waveforms in LAD explains the from-moderately-to-scarcely multidirectional nature of **WSS**, already emerged in previous studies evaluating hemodynamic descriptors of **WSS** multidirectionality.[13] However, our *"layered"* analysis on **WSS**$_{sc}$ time-histories highlights that, although **WSS**$_{sc}$ magnitude scarcely contributes to the overall **WSS** vector

**Table 2.** Summary of the main findings of the correlation-based analysis and CNs study.

| Emergent features of LAD hemodynamics |
|---|
| **"*all-to-all*" correlation analysis**<br>– Predominance of forward blood flow with minimal flow reversal leads to highly correlated $\|\mathbf{WSS}\|$ and $\mathbf{WSS}_{ax}$ time-histories<br>– $\mathbf{WSS}_{sc}$ time-histories are either markedly positively or negatively correlated<br>– Uncorrelated $WSS_{ratio}$ waveforms at the luminal surface are localized in regions where $\|\mathbf{WSS}_{sc}\|$ is, on average, comparable to or higher than $\|\mathbf{WSS}_{ax}\|$ |
| **"*layered*" correlation analysis**<br>– Correlation patterns at the luminal surface are markedly affected by the $\mathbf{WSS}_{sc}$ directionality<br>– Alternance of regions at the luminal surface where $\mathbf{WSS}_{sc}$ and $\mathbf{WSS}_{ax}$ are "in phase" or "out-of-phase" |
| **"*one-to-all*" correlation analysis**<br>– The LAD inlet flow-rate waveform markedly shapes $\|\mathbf{WSS}\|$ and $\mathbf{WSS}_{ax}$ time-histories |
| **CNs analysis**<br>– At the inner wall, $\|\mathbf{WSS}\|$ and $\mathbf{WSS}_{ax}$ time-histories are different from the rest of the luminal surface<br>– $\mathbf{WSS}_{sc}$ time-histories feature: presence of two distinguishable, large spatiotemporally correlated structures on the luminal surface<br>– In $\mathbf{WSS}_{sc}$ networks, connections between time-histories are overall more compact and stable (low $\overline{SPL}$ values and low inter-variability)<br>– In $\|\mathbf{WSS}\|$, $\mathbf{WSS}_{ax}$ and $WSS_{ratio}$ networks, topologically isolated regions (low $DC$ and $\overline{SPL}$) co-localize with low cycle-average $\|\mathbf{WSS}\|$ |

LAD: left anterior descending; WSS: wall shear stress.

(Figure 3), the dynamics of $\mathbf{WSS}_{sc}$ can be strongly (high $R_{ij}$ absolute values) correlated or anti-correlated with the dynamics of $\mathbf{WSS}_{ax}$ and $|\mathbf{WSS}|$ (Figure 5, and Figure S4 bottom panel in the Supplementary Data).

Moreover, strong correlations are also found between $\mathbf{WSS}_{sc}$ time-histories, as highlighted by the *"all-to-all"* analysis (Figure 4 bottom-left panel). These correlations translate in markedly compact topological connections between time-histories in the $\mathbf{WSS}_{sc}$-based CNs. In fact, both $DC$ and $\overline{SPL}$ distributions (Figures 8 and 10) do not highlight luminal surface areas where the dynamic behavior of $\mathbf{WSS}_{sc}$ time-histories markedly differs from the rest of the vessel wall (i.e. the overall distributions of $DC$ and $\overline{SPL}$ are almost uniform, on the luminal surface). This emergent highly compact topological feature looks very similar to that of helicity-based CNs analyzed in a recent study on human carotid bifurcation hemodynamics,[19] and in agreement with very recent findings on the role of the rotating direction of helical flow patterns in dictating the luminal distribution of $\mathbf{WSS}_{sc}$ in coronary arteries.[13] The results from this study suggest that both the $\mathbf{WSS}_{sc}$ dynamics along the cardiac cycle and its distribution at the luminal surface are markedly dictated by the bi-helical intravascular blood flow patterns in the LAD.[13] For these reasons, and since an atheroprotective role has been suggested for bi-helical flow patterns in coronary arteries,[13] the spatiotemporal features of $\mathbf{WSS}_{sc}$ waveforms and their association with helical flow deserve further investigation.

The CNs-based analysis of $|\mathbf{WSS}|$ and $\mathbf{WSS}_{ax}$ time-histories highlights that the spatiotemporal "complexity" of those "networks" is characterized by well-distinct, topologically isolated regions (Figures 7 and 10), preferentially located at the LAD inner wall. Here, the persistence length of correlations is shorter than elsewhere at the LAD luminal surface, since the topological path separating the nodes is longer (high $\overline{SPL}$). The same topological features characterize also $WSS_{ratio}$-based networks (Figures 9 and 10).

Notably, the dynamically isolated regions highlighted by the CNs, where time-histories are markedly different in shape from the rest of the vessel, in general are always co-localized with low cycle-average $|\mathbf{WSS}|$ (Figures 7, 9 and 10). This finding suggests that not only the magnitude of the cycle-average $|\mathbf{WSS}|$ plays a main role in the initiation of the disease,[1,5,6,14,15] but also the shape of the WSS time-histories, as well as the shape of the ratio between the secondary and the axial **WSS** projections, could contribute to trigger atherosclerosis at its earliest stage. According to this hypothesis, different shapes of WSS waveforms could trigger different mechanobiological responses on the ECs. This conclusion echoes previous observations suggesting different mechanobiological implications to the exposure to WSS-based quantities with distinct waveforms. In other words, the present findings suggest that atheroprotective versus atheroprone waveform shapes can be discriminated and that the latter are more heterogeneous.[36]

## Conclusion

In conclusion, we performed an exploratory study on personalized pig models of LAD, combining correlation-based analysis and CNs theory with computational hemodynamics. The main findings of this work suggest that where the **WSS** is low in magnitude, the time-histories of WSS-based descriptors are markedly different in shape from elsewhere in the vessel and have a short topological correlation length. Reminding the widely recognized atheroprone action of low **WSS** magnitude on the endothelium, the present results of the CNs analysis lay the groundwork for future research about the role of the shape of **WSS** temporal variations in inducing the biological events triggering atherosclerotic coronary disease, in the context of the so-called hemodynamic risk hypothesis. This may support the identification of atheroprone versus atheroprotective WSS waveforms and the *in vitro* study of their effect on the distinct modulation of ECs phenotype.[36] In this perspective, the present study could open new avenues for a more comprehensive characterization of the link between **WSS** and atherosclerosis.

## Declaration of conflicting interests

The author(s) declared no potential conflicts of interest with respect to the research, authorship and/or publication of this article.

## Funding

The author(s) received no financial support for the research, authorship and/or publication of this article.

## ORCID iDs

Karol Calò https://orcid.org/0000-0002-6935-4021
Umberto Morbiducci https://orcid.org/0000-0002-9854-1619

## Supplemental material

Supplemental material for this article is available online.

## References

1. Morbiducci U, Kok AM, Kwak BR, et al. Atherosclerosis at arterial bifurcations: evidence for the role of haemodynamics and geometry. *Thromb Haemost* 2016; 115(3): 484–492.
2. Caro CG, Fitz-Gerald JM and Schroter RC. Atheroma and arterial wall shear. Observation, correlation and proposal of a shear dependent mass transfer mechanism for atherogenesis. *Proc R Soc Lond B Biol Sci* 1971; 177(1046): 109–159.
3. Zarins CK, Giddens DP, Bharadvaj BK, et al. Carotid bifurcation atherosclerosis. Quantitative correlation of plaque localization with flow velocity profiles and wall shear stress. *Circ Res* 1983; 53(4): 502–514.
4. Ku DN, Giddens DP, Phillips DJ, et al. Hemodynamics of the normal human carotid bifurcation: in vitro and in vivo studies. *Ultrasound Med Biol* 1985; 11(1): 13–26.
5. Koskinas KC, Sukhova GK, Baker AB, et al. Thin-capped atheromata with reduced collagen content in pigs develop in coronary arterial regions exposed to persistently low endothelial shear stress. *Arterioscler Thromb Vasc Biol* 2013; 33(7): 1494–1504.
6. Stone PH, Saito S, Takahashi S, et al. Prediction of progression of coronary artery disease and clinical outcomes using vascular profiling of endothelial shear stress and arterial plaque characteristics: the PREDICTION study. *Circulation* 2012; 126: 172–181.
7. Peiffer V, Sherwin SJ and Weinberg PD. Computation in the rabbit aorta of a new metric–the transverse wall shear stress–to quantify the multidirectional character of disturbed blood flow. *J Biomech* 2013; 46(15): 2651–2658.
8. Gallo D, Bijari PB, Morbiducci U, et al. Segment-specific associations between local haemodynamic and imaging markers of early atherosclerosis at the carotid artery: an in vivo human study. *J R Soc Interface* 2018; 15: 20180352.
9. Martorell J, Santomá P, Kolandaivelu K, et al. Extent of flow recirculation governs expression of atherosclerotic and thrombotic biomarkers in arterial bifurcations. *Cardiovasc Res* 2014; 103(1): 37–46.
10. Mohamied Y, Rowland EM, Bailey EL, et al. Change of direction in the biomechanics of atherosclerosis. *Ann Biomed Eng* 2015; 43(1): 16–25.
11. Morbiducci U, Gallo D, Cristofanelli S, et al. A rational approach to defining principal axes of multidirectional wall shear stress in realistic vascular geometries, with application to the study of the influence of helical flow on wall shear stress directionality in aorta. *J Biomech* 2015; 48(6): 899–906.
12. Gallo D, Steinman DA and Morbiducci U. Insights into the co-localization of magnitude-based versus direction-based indicators of disturbed shear at the carotid bifurcation. *J Biomech* 2016; 49(12): 2413–2419.
13. De Nisco G, Kok AM, Chiastra C, et al. The atheroprotective nature of helical flow in coronary arteries. *Ann Biomed Eng* 2019; 47(2): 425–438.
14. Chatzizisis YS, Coskun AU, Jonas M, et al. Role of endothelial shear stress in the natural history of coronary atherosclerosis and vascular remodeling. *J Am Coll Cardiol* 2007; 49: 2379–2393.
15. Wentzel JJ, Chatzizisis YS, Gijsen FJH, et al. Endothelial shear stress in the evolution of coronary atherosclerotic plaque and vascular remodelling: current understanding and remaining questions. *Cardiovasc Res* 2012; 96: 234–243.
16. Wang C, Baker BM, Chen CS, et al. Endothelial cell sensing of flow direction. *Arterioscler Thromb Vasc Biol* 2013; 33(9): 2130–2136.
17. Hoogendoorn A, Kok AM, Hartman EMJ, et al. Multidirectional wall shear stress promotes advanced coronary plaque development: comparing five shear stress metrics. *Cardiovasc Res* 2019; cvz212: 1–11.
18. Kok AM, Molony DS, Timmins LH, et al. The influence of multidirectional shear stress on plaque progression and composition changes in human coronary arteries. *Eurointervention* 2019; 15: 692–699.
19. Calò K, Gallo D, Steinman DA, et al. Spatiotemporal hemodynamic complexity in carotid arteries: an integrated computational hemodynamics & complex networks-based approach. *IEEE Trans Biomed Eng*. Epub ahead of print 23 October 2019. DOI: 10.1109/TBME.2019.2949148.
20. Boccaletti S, Latora V, Moreno Y, et al. Complex networks: structure and dynamics. *Phys Rep* 2006; 424: 175–308.
21. Sun J, Yang Y, Xiong NN, et al. Complex network construction of multivariate time series using information geometry. *IEEE Trans Syst Man Cyber Syst* 2019; 49: 107–122.
22. Taira K, Nair AG and Brunton SL. Network structure of two-dimensional decaying isotropic turbulence. *J Fluid Mech* 2016; 795: R2.
23. Scarsoglio S, Iacobello G and Ridolfi L. Complex networks unveiling spatial patterns in turbulence. *Int J Bifurc Chaos* 2016; 26: 1650223.
24. Liu C, Zhou WX and Yuan WK. Statistical properties of visibility graph of energy dissipation rates in three-dimensional fully developed turbulence. *Phys A Stat Mech Appl* 2010; 389(13): 2675–2681.
25. Iacobello G, Scarsoglio S, Kuerten JGM, et al. Spatial characterization of turbulent channel flow via complex networks. *Phys Rev E* 2018; 98: 13107.
26. National Research Council. Committee for the update of the guide for the care and use of laboratory animals. In: National Research Council (ed.) *Guide for the care and use of laboratory animals*. 8th ed. Washington, DC: National Academies Press, 2011.

27. Chiastra C, Gallo D, Tasso P, et al. Healthy and diseased coronary bifurcation geometries influence near-wall and intravascular flow: a computational exploration of the hemodynamic risk. *J Biomech* 2017; 58: 79–88.
28. Gijsen FJH, Allanic E, van de Vosse FN, et al. The influence of the non-Newtonian properties of blood on the flow in large arteries: unsteady flow in a 90° curved tube. *J Biomech* 1999; 32(7): 705–713.
29. Morbiducci U, Gallo D, Massai D, et al. On the importance of blood rheology for bulk flow in hemodynamic models of the carotid bifurcation. *J Biomech* 2011; 44: 2427–2438.
30. Arzani A. Accounting for residence-time in blood rheology models: do we really need non-Newtonian blood flow modelling in large arteries? *J R Soc Interface* 2018; 15(146): 20180486.
31. Malvè M, García A, Ohayon J, et al. Unsteady blood flow and mass transfer of a human left coronary artery bifurcation: FSI vs. CFD. *Int Commun Heat Mass Transf* 2012; 39: 745–751.
32. Huo Y and Kassab GS. Intraspecific scaling laws of vascular trees. *J R Soc Interface* 2012; 9(66): 190–200.
33. Chatzizisis YS, Jonas M, Coskun AU, et al. Prediction of the localization of high-risk coronary atherosclerotic plaques on the basis of low endothelial shear stress: an intravascular ultrasound and histopathology natural history study. *Circulation* 2008; 117(8): 993–1002.
34. Gijsen F, Katagiri Y, Barlis P, et al. Expert recommendations on the assessment of wall shear stress in human coronary arteries: existing methodologies, technical considerations, and clinical applications. *Eur Heart J* 2019; 40: 3421–3433.
35. Stone PH, Maehara A, Coskun AU, et al. Role of low endothelial shear stress and plaque characteristics in the prediction of nonculprit major adverse cardiac events: the PROSPECT study. *JACC Cardiovasc Imaging* 2018; 11(3): 462–471.
36. Dai G, Kaazempur-Mofrad MR, Natarajan S, et al. Distinct endothelial phenotypes evoked by arterial waveforms derived from atherosclerosis-susceptible and -resistant regions of human vasculature. *Proc Natl Acad Sci U S A* 2004; 101(41): 14871–14876.